



CHALMERS
UNIVERSITY OF TECHNOLOGY

Gold-activated persulfate p-doping of organic semiconductors

Downloaded from: <https://research.chalmers.se>, 2026-04-14 10:06 UTC

Citation for the original published paper (version of record):

Liu, T., Silveri, M., Liu, Z. et al (2026). Gold-activated persulfate p-doping of organic semiconductors. Nature Materials, In Press. <http://dx.doi.org/10.1038/s41563-026-02547-0>

N.B. When citing this work, cite the original published paper.

Gold-activated persulfate p-doping of organic semiconductors

Received: 26 June 2025

Accepted: 11 February 2026

Published online: 17 March 2026

Check for updates

Tiefeng Liu^{1,2}, Matilde Silveri¹, Zesheng Liu¹, Sang Young Jeong³, Qiao He⁴, Giannis G. Gkikas⁵, Wenlong Jin¹, Chi-Yuan Yang¹, Tom P. A. van der Pol¹, Feng Zhang¹, Christina Kousseff⁶, Anna Martinelli⁵, Iain McCulloch^{6,7}, Martin Heeney⁸, Han Young Woo³, Alessandro Motta⁹, Mats Fahlman¹ & Simone Fabiano^{1,2}✉

Chemical doping is crucial for fine-tuning the electronic properties of organic semiconductors (OSCs) and enhancing device performance across various technologies. While several methods for controlled dopant distribution have been explored, achieving lateral doping gradients via simple solution processing remains challenging. Here we present a gold-activated persulfate doping strategy in which persulfate is catalytically activated at gold surfaces to generate $\text{SO}_4^{\cdot-}$ radicals that locally oxidize (p-dope) the OSCs. This reaction creates a lateral doping gradient extending outwards from the gold interface, as verified by spectroscopic and electrical characterization. The approach is broadly applicable to OSCs spanning a 1.5-eV ionization potential range and yields conductivities $>1,900 \text{ S cm}^{-1}$. To demonstrate the impact of this method, we applied gold-activated persulfate doping to modulate contact regions in solution-processed organic field-effect transistors, achieving reduced contact resistance and improved charge-carrier mobility. This simple, scalable approach enables the formation of lateral doping gradients from solution and offers new opportunities for interfacial tuning in organic electronics.

Chemical doping is a key process in organic semiconductors (OSCs), used to tailor their electronic properties^{1,2} and enhance device performance in applications such as solar cells^{3,4}, light-emitting diodes^{5,6}, thermoelectrics^{7,8}, transistors^{9,10} and electrochemical systems^{11,12}. Advances in dopant design and doping strategies have enabled conductivities exceeding 10^3 S cm^{-1} (refs. 13–17). Conventional doping methods typically involve either coprocessing (for example, co-blending in solution or co-evaporation) or sequential deposition (for example, spin-coating or vapour-depositing the

dopant onto a preformed OSC film), both of which generally lead to uniformly doped films¹⁸. However, the ability to locally dope specific regions of OSCs via wet processing remains an open challenge, with major implications for enhancing device performance across a wide range of technologies, including solution-processed organic field-effect transistors (OFETs)^{19,20}, organic electrochemical transistors^{21,22}, organic thermoelectric generators²³ and other applications where precise doping of the OSC/contact regions is critical for optimal operation^{24,25}.

¹Laboratory of Organic Electronics, Department of Science and Technology, Linköping University, Norrköping, Sweden. ²Wallenberg Initiative Materials Science for Sustainability, Department of Science and Technology, Linköping University, Norrköping, Sweden. ³Department of Chemistry, College of Science, Korea University, Seoul, Republic of Korea. ⁴College of Education Sciences, The Hong Kong University of Science and Technology (Guangzhou), Guangzhou, China. ⁵Department of Chemistry and Chemical Engineering, Chalmers University of Technology, Gothenburg, Sweden. ⁶Department of Chemistry, University of Oxford, Oxford, UK. ⁷Andlinger Center for Energy and the Environment and Department of Electrical and Computer Engineering, Princeton University, Princeton, NJ, USA. ⁸Physical Sciences and Engineering Division, King Abdullah University of Science and Technology, Thuwal, Kingdom of Saudi Arabia. ⁹Dipartimento di Scienze Chimiche, Università di Roma 'La Sapienza' and INSTM, Udr Roma, Rome, Italy.

✉e-mail: simone.fabiano@liu.se

Various strategies for spatially modulating dopant distribution have been explored, including laser patterning^{26,27}, dopant deposition via thermal evaporation^{28,29} or printing^{30,31}, light-assisted doping^{32,33} and electrochemical ion implantation³⁴. While effective, these approaches often rely on energy-intensive or technically demanding conditions, limiting their scalability. By contrast, achieving spatial modulation of doping levels through solution processing remains difficult. Although vertical doping gradients have been demonstrated using kinetically controlled doping in solution with bulky molecular dopants³⁵, achieving lateral gradients in dopant distribution via solution processing remains an unresolved challenge.

Here, we introduce a gold-activated persulfate (GAP) doping strategy that enables the formation of lateral doping gradients in OSCs from solution. We show that persulfate is catalytically activated upon contact with gold, generating $\text{SO}_4^{\cdot-}$ radicals that strongly oxidize (p-dope) OSCs, as schematically illustrated in Fig. 1a. This localized activation leads to a lateral doping gradient, as confirmed by spatially resolved optical spectroscopy. The method is applicable to a variety of p-type OSCs with ionization potentials (IPs) spanning a 1.5-eV range and achieves electrical conductivities exceeding $1,900 \text{ S cm}^{-1}$. To demonstrate the potential of this approach, we used GAP to modulate the OSC's doping level at the source/drain contact regions in OFETs, reducing contact resistance by $\sim 10\times$ at low gate bias and doubling carrier mobility. By enabling simple, scalable formation of lateral doping gradients from solution, this approach offers new opportunities for interfacial tuning and performance enhancement in next-generation organic electronic devices.

GAP doping of PBTTT

Sodium persulfate ($\text{Na}_2\text{S}_2\text{O}_8$; Fig. 1b) is a potent and air-stable oxidizing agent, commonly used for soil and groundwater remediation³⁶, as well as a polymerization initiator in the synthesis of both commodity³⁷ and conjugated³⁸ polymers. However, when poly(2,5-bis(3-hexadecylthiophen-2-yl)thieno[3,2-*b*]thiophene) (PBTTT) films deposited on glass substrates were immersed in a 10-mM $\text{Na}_2\text{S}_2\text{O}_8$ solution, only minimal doping was observed. The ultraviolet–visible–near-infrared spectra showed a slight reduction in the neutral absorption peak at $\sim 550 \text{ nm}$ and a modest increase in polaron absorption in the 700–1,000-nm region (Fig. 1c). By contrast, PBTTT films deposited on gold-coated glass and exposed to the same doping conditions exhibited complete bleaching of the neutral peak and a strong polaron absorption band centred around $\sim 820 \text{ nm}$, extending into the infrared region (Fig. 1c; see optical photographs in Supplementary Fig. 1). Quartz crystal microbalance with dissipation monitoring (QCM-D) measurements confirmed that persulfate solution penetrates PBTTT films (Supplementary Fig. 2), indicating that the limited doping on glass is not due to poor diffusion but rather to the low oxidation efficiency of $\text{Na}_2\text{S}_2\text{O}_8$ alone, consistent with previous reports that used persulfate with other polymer systems in the absence of gold^{39,40}. Passivating the gold surface with a self-assembled monolayer of 1-dodecanethiol (DDT) hindered the emergence of the polaron bands in the absorption spectra (Fig. 1d). However, when subjected to thermal annealing at 180°C , a process known to cause desorption of DDT from gold⁴¹, the samples exhibited full bleaching of the neutral peak and strong polaron absorption at wavelengths above 650 nm (Fig. 1d). These observations indicate that a clean gold surface plays a critical role in enabling the doping process. Other metals commonly used in organic electronic devices, such as chromium and copper, also supported GAP doping, while aluminium and silver showed only minimal effects (Supplementary Fig. 3), probably due to surface reactions (oxidation, passivation and/or leaching) that interfere with sustained radical generation at the metal–OSC interface.

In parallel with the optical changes, a substantial difference in electrical conductivity was observed when comparing bare gold electrodes with either DDT-modified gold or indium tin oxide (ITO)

electrodes (Fig. 1e). PBTTT films with bare gold electrodes showed a rapid increase in conductivity within 10 s, reaching a maximum of $965 \pm 59 \text{ S cm}^{-1}$ after approximately 30 s, consistent with the rapid colour change observed in Supplementary Video 1. Note that the conductivity remained well above 200 S cm^{-1} even after 235 h of storage under ambient conditions (Extended Data Fig. 1). Lower dopant concentrations led to slower doping kinetics, as shown in Extended Data Fig. 2. For comparison, PBTTT films doped using $\text{F}_4\text{TCNQ/ion}$ exchange reached a substantially lower maximum conductivity of $563 \pm 39 \text{ S cm}^{-1}$ (Supplementary Fig. 4), a value consistent with previous reports⁴². By contrast, persulfate-doped PBTTT films using ITO or DDT-modified gold electrodes exhibited conductivities three to four orders of magnitude lower ($0.40 \pm 0.19 \text{ S cm}^{-1}$ for ITO and $0.049 \pm 0.018 \text{ S cm}^{-1}$ for DDT-modified gold; Fig. 1e and Supplementary Fig. 5). It should be noted that the lower conductivity observed for PBTTT on DDT-modified gold, compared with that on ITO, is probably due to the absence of thermal annealing, which was deliberately avoided to prevent DDT desorption. Indeed, annealing removes the DDT layer, reactivates the gold surface and restores conductivity to levels comparable to those of unmodified gold electrodes (Fig. 1e).

Other persulfate salts, such as potassium persulfate ($\text{K}_2\text{S}_2\text{O}_8$) and ammonium persulfate ($(\text{NH}_4)_2\text{S}_2\text{O}_8$), were also able to dope PBTTT in the presence of bare gold electrodes, yielding conductivities of 653 ± 37 and $611 \pm 22 \text{ S cm}^{-1}$, respectively (Supplementary Fig. 6). All electrical conductivity measurements were performed in the presence of lithium bis(trifluoromethanesulfonyl)imide (LiTFSI), dissolved in the same acetonitrile solution, with TFSI⁻ ions serving as counterions to balance the positive charge on the PBTTT chains. LiTFSI itself has no doping ability, as confirmed by negligible changes in absorbance and conductivity (Supplementary Fig. 7).

Even in the absence of LiTFSI, PBTTT films doped with $\text{Na}_2\text{S}_2\text{O}_8$ on bare gold electrodes still reached relatively high doping levels, as indicated by bleaching of the neutral peak, emergence of the polaron band and conductivities exceeding 100 S cm^{-1} (Extended Data Fig. 3). The addition of LiTFSI, however, increases conductivity by nearly an order of magnitude. LiTFSI does not induce doping but promotes a spontaneous $\text{SO}_4^{2-}/\text{TFSI}^-$ counterion-exchange process, as supported by density functional theory (DFT) calculations, which show the exchange to be exothermic and therefore thermodynamically favourable (Extended Data Fig. 4), consistent with earlier observation of rapid anion exchange in doped OSCs⁴². Importantly, the doping kinetics are nearly identical with or without TFSI⁻ (Fig. 1e and Extended Data Fig. 3b), demonstrating that counterion exchange is not the rate-limiting step. Instead, the doping rate is strongly dependent on OSC film thickness, with thicker films requiring longer times to reach saturation conductivity and fully bleach the neutral absorption peak (Extended Data Fig. 5 and Supplementary Fig. 8), indicating that GAP doping is probably limited by the diffusion of persulfate throughout the bulk of the OSC layer. Overall, these results indicate that TFSI⁻ acts as a stabilizing counterion that facilitates ion exchange and thereby substantially enhances the overall efficiency of the GAP doping process without altering the doping kinetics.

To investigate the role of gold in promoting the doping of PBTTT by persulfate, we conducted X-ray photoelectron spectroscopy (XPS) measurements. As shown in Fig. 1f, the sulfur S(2*p*) signal of undoped PBTTT spin-cast on a gold-coated glass substrate exhibits two symmetrical peaks at 164.0 eV and 165.2 eV, corresponding to the spin-split doublet ($2p_{3/2}$ and $2p_{1/2}$) of the sulfur atom in the thiophene ring. After exposure to $\text{Na}_2\text{S}_2\text{O}_8/\text{LiTFSI}$ solution, the S(2*p*) peaks of PBTTT shift to lower binding energy and display an asymmetric tail extending towards higher binding energy. This asymmetry suggests the formation of positive charges (polarons/bipolarons) delocalized along the PBTTT backbone, reflecting changes in the electronic environment near the sulfur atom^{43,44}. In addition, a strong S(2*p*) signal

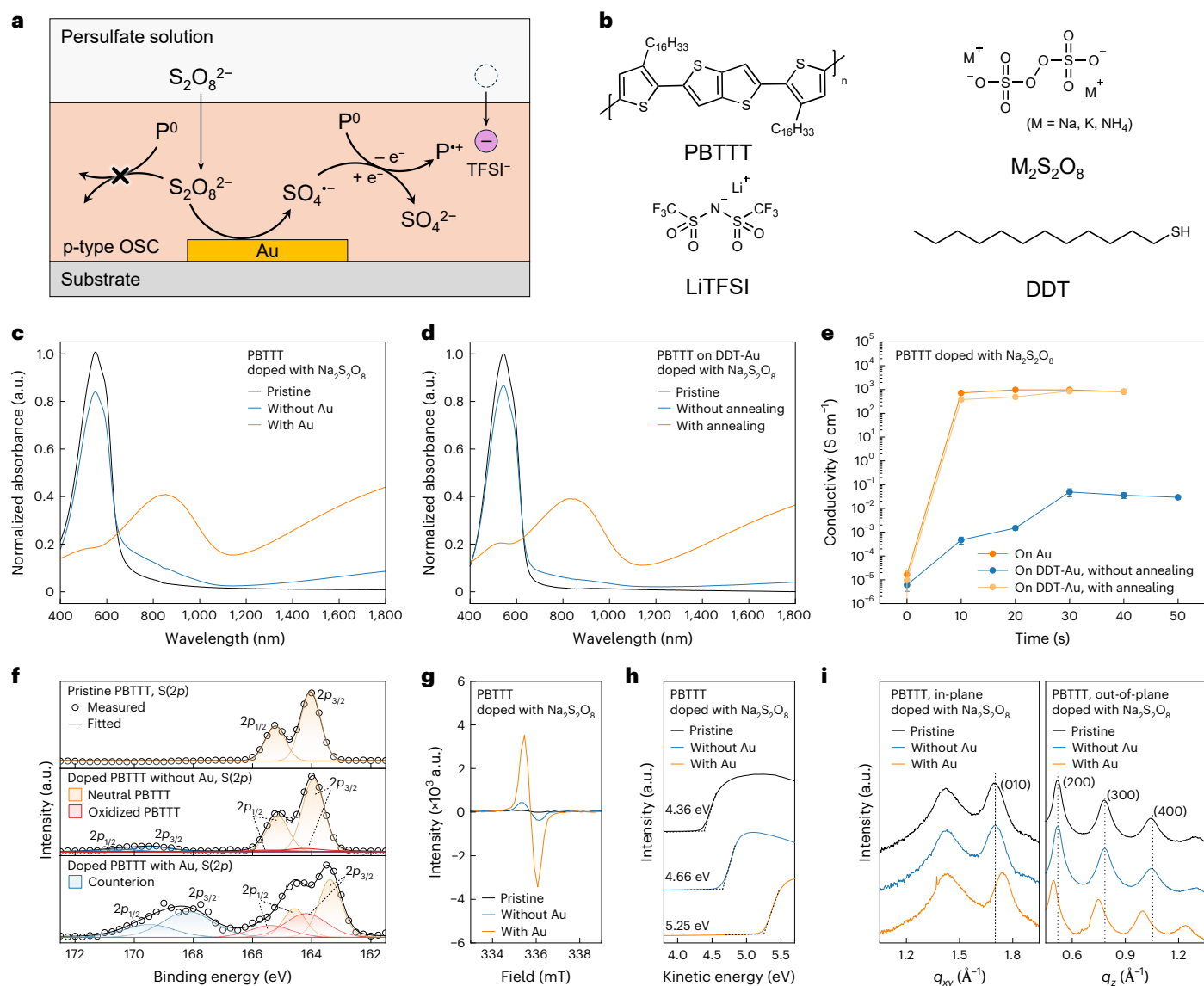


Fig. 1 | **GAP doping of PBTTT.** **a, b**, Schematic illustration of the GAP doping method (**a**), along with the chemical structures of the persulfate dopant, LiTFSI counterion, PBTTT and DDT (**b**). **c**, Absorption spectra of PBTTT films deposited on bare glass and gold-coated glass substrates after doping with $\text{Na}_2\text{S}_2\text{O}_8$. **d**, Absorption spectra of PBTTT films deposited on DDT-modified gold substrates upon doping with $\text{Na}_2\text{S}_2\text{O}_8$ before and after thermal annealing at 180°C , a process that causes deprotection of the gold surface. **e**, Electrical conductivity of PBTTT films measured using bare gold or DDT-modified gold electrode after doping

with $\text{Na}_2\text{S}_2\text{O}_8$. Points represent mean values; error bars show standard deviation (s.d., not visible at this scale); $n = 10$ independent samples. **f**, $\text{S}(2p)$ XPS spectra of undoped and persulfate-doped PBTTT films with and without gold. **g**, EPR spectra of undoped and persulfate-doped PBTTT films with and without gold. **h**, UPS spectra of undoped and persulfate-doped PBTTT films with and without gold. **i**, GIWAXS line cuts of undoped and persulfate-doped PBTTT films with and without gold.

attributed to counterions appears at 167–171 eV, along with distinct nitrogen N(1s) and fluorine F(1s) signals (Supplementary Fig. 9). By contrast, when PBTTT films were exposed to $\text{Na}_2\text{S}_2\text{O}_8/\text{LiTFSI}$ solution without an underlying gold layer, the $\text{S}(2p)$ peaks remained largely unchanged and the TFSI⁻ signal was weak, indicating a substantially lower doping level. To quantify the doping level, the PBTTT $\text{S}(2p)$ region was fitted with two doublets corresponding to neutral and oxidized polythiophene¹⁶. The estimated doping levels were 45% with gold, 11% without gold and 12% with DDT-modified gold (see Extended Data Fig. 6 for the latter), calculated as the ratio of the oxidized PBTTT doublet area to the total area of both oxidized and neutral components. The increase in charge density correlates with the higher conductivity and lower Seebeck coefficient measured for PBTTT films doped on bare gold electrodes (Fig. 1e and Supplementary Fig. 10). For comparison, PBTTT films doped via F_4TCNQ /ion exchange exhibited a doping

level of 33% (Supplementary Fig. 11), consistent with their lower conductivity (Supplementary Fig. 4). These trends are further supported by electron paramagnetic resonance (EPR) measurements, which showed a strong signal only when gold was present (Fig. 1g), and by ultraviolet photoelectron spectroscopy (UPS) measurements, where PBTTT films deposited on gold exhibited a greater shift in the secondary electron cut-off and a higher work function (5.25 eV versus 4.66 eV; Fig. 1h). In addition, the near alignment of the valence band edge with the Fermi level confirmed a heavily doped state in PBTTT films on gold (Supplementary Fig. 12).

Grazing-incidence wide-angle X-ray scattering (GIWAXS) provided further structural evidence. Both pristine and doped PBTTT films exhibited an edge-on orientation on gold-coated and bare silicon substrates (Fig. 1i). However, only the doped films on gold showed notable structural changes: the π - π stacking peak shifted from $q_{xy} = 1.697$ to 1.742 \AA^{-1}

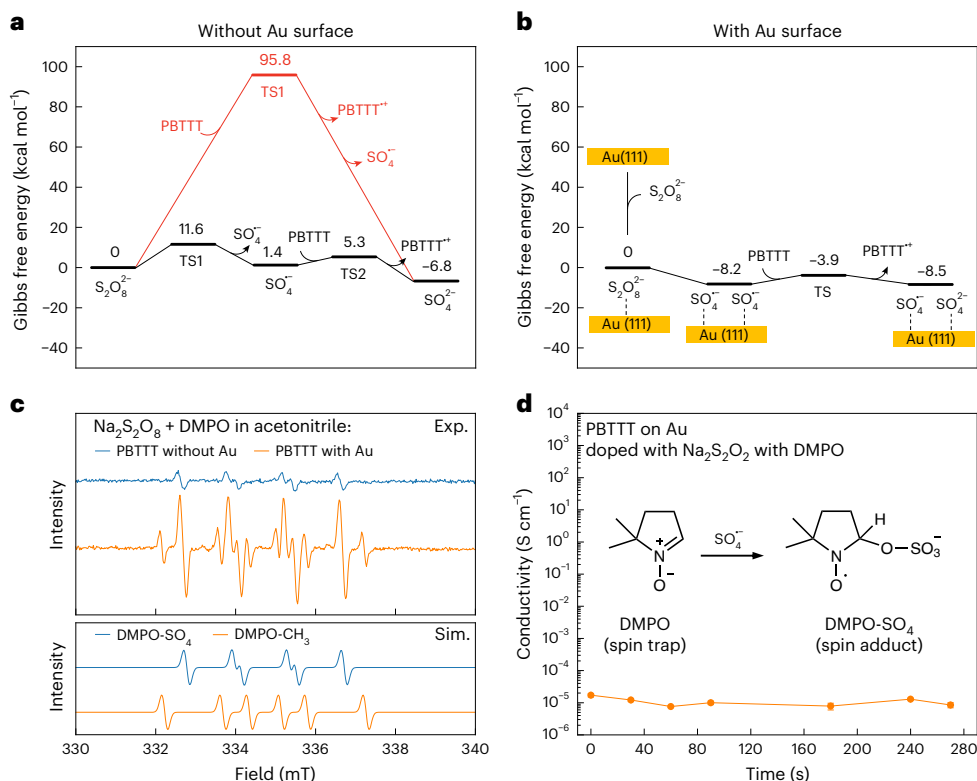


Fig. 2 | Mechanism of GAP doping process. **a, b**, DFT-calculated Gibbs free energy profiles for the reaction of persulfate with PBTTT in the absence (**a**) and presence (**b**) of a gold surface. In **a**, both a direct electron-transfer pathway (red line) and a two-step radical-mediated mechanism (black line) were considered. **c**, EPR spectra of Na₂S₂O₈ solution in contact with a PBTTT film using DMPO as a spin trap, confirming the presence of SO₄⁻ radicals. Simulated (Sim.) spectra are

shown for comparison and exhibit good agreement with the experimental (Exp.) data. **d**, Electrical conductivity of PBTTT films doped with Na₂S₂O₈ in the presence of DMPO, showing suppression of doping due to radical scavenging. The chemical structures of DMPO and its adduct with SO₄⁻ are reported in **d**. Points represent mean values; error bars show standard deviation (s.d., not visible at this scale); *n* = 10 independent samples.

(corresponding to a reduced stacking distance from 3.70 to 3.61 Å), and the lamellar peak shifted from $q_z = 0.781$ to 0.748 \AA^{-1} (increased spacing from 24.14 to 25.20 Å), consistent with the incorporation of TFSI⁻ counterions in the side-chain region^{13,15}. By contrast, films doped on bare silicon exhibited only minimal structural changes, indicating weak oxidation in the absence of gold (Supplementary Figs. 13 and 14 and Supplementary Table 1). Taken together, the XPS, EPR, UPS and GIWAXS results provide compelling evidence that the presence of gold during doping enables markedly more efficient oxidation of PBTTT with persulfate.

Mechanism of GAP doping

To gain mechanistic insight into the gold-assisted doping of PBTTT by Na₂S₂O₈, we performed DFT calculations to identify the most energetically favourable charge-transfer pathway, both with and without a gold surface. In the absence of gold, two possible doping mechanisms were considered (Fig. 2a). The first involves direct electron transfer between S₂O₈²⁻ and PBTTT (red curve), resulting in the formation of a radical species (S₂O₈^{-•}), which spontaneously dissociates into SO₄⁻ and SO₄⁻. The second is a two-step process (black curve), where S₂O₈²⁻ undergoes homolytic cleavage to yield two SO₄⁻ radicals, followed by electron transfer between one of the radicals and the PBTTT chain. The energy profiles indicate that the direct pathway is less favourable, with a substantially higher activation barrier than the two-step route. These results align with previous reports⁴⁵, highlighting the ease with which symmetric S₂O₈²⁻ dissociates into radical species in solution.

Given this preference, we next modelled the two-step mechanism in the presence of a gold surface (Fig. 2b). Remarkably, adsorption of S₂O₈²⁻ onto gold substantially lowers the energy barriers for both

homolytic cleavage and subsequent electron transfer, with the cleavage step becoming entirely barrierless. This catalytic effect is probably due to gold's ability to stabilize the radical intermediates and delocalize the excess charge resulting from the oxidation of PBTTT. Thus, the presence of gold not only facilitates the generation of reactive sulfate radicals but also lowers the overall energetic cost of the doping process. These theoretical findings support our experimental observations and confirm the critical role of gold as a catalyst in the activation of persulfate dopants. In the absence of gold, doping is inefficient; in its presence, radical generation and electron transfer proceed readily. Although the fate of the sulfate species after electron transfer has not been investigated, our results provide compelling evidence for a gold-assisted radical-doping mechanism.

The presence of SO₄⁻ radicals was confirmed by EPR spectroscopy using 5,5-dimethyl-1-pyrroline-*N*-oxide (DMPO), a spin trap that forms stable nitroxide adducts with radical species. As shown in Fig. 2c, the EPR spectrum of Na₂S₂O₈ solution in the presence of PBTTT film on gold exhibits four prominent peaks with an intensity ratio of 1:1:1:1 and hyperfine coupling constants of $\alpha_N = 1.35 \text{ mT}$ and $\alpha_H = 1.20 \text{ mT}$. These values are consistent with those reported for the DMPO-SO₄ adduct^{46,47}, confirming the generation of SO₄⁻ radicals. In addition, six weaker peaks of equal intensity were observed, characterized by hyperfine coupling constants of $\alpha_N = 1.46 \text{ mT}$ and $\alpha_H = 2.12 \text{ mT}$. These values correspond to the DMPO-CH₃ adduct⁴⁸, probably resulting from acetonitrile degradation induced by the highly reactive SO₄⁻ radicals⁴⁹. The experimental spectra closely match the simulated results (Fig. 2c). Notably, the EPR spectra of the same solution in the presence of PBTTT but without gold showed similar peak patterns but with markedly lower intensity, indicating a reduced concentration of SO₄⁻ radicals formed

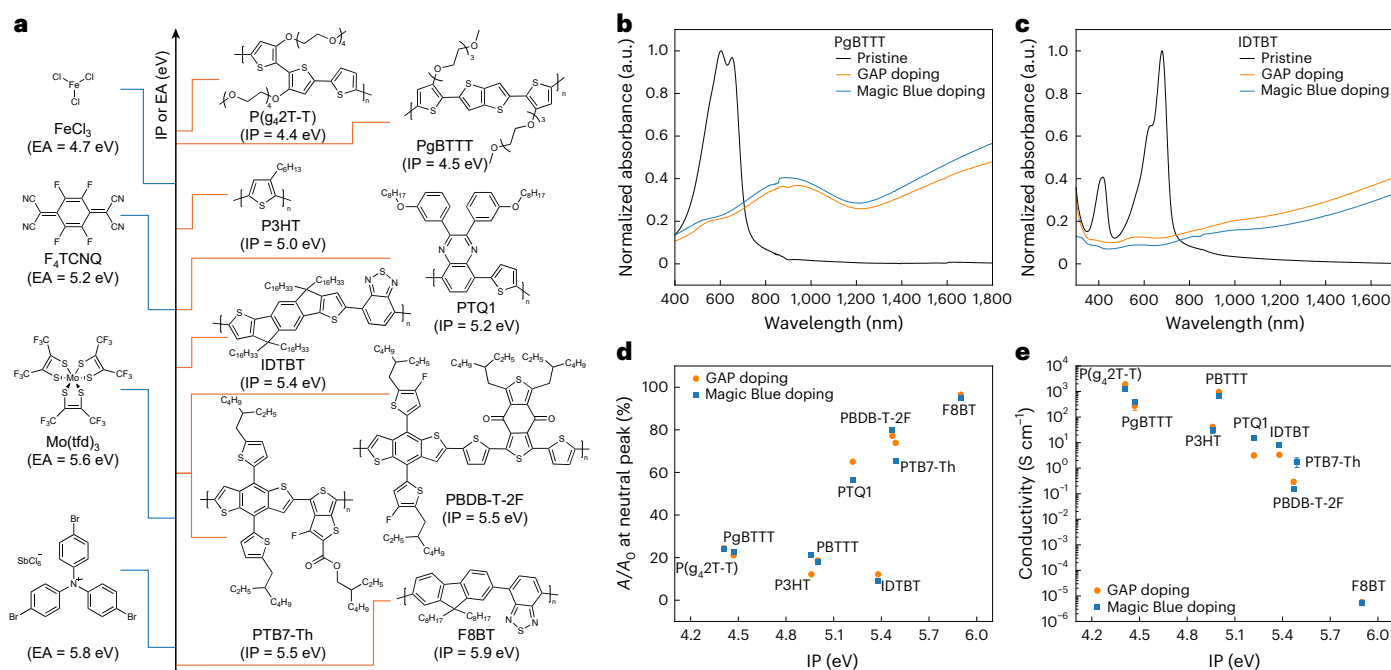


Fig. 3 | Generality of the GAP doping process. **a**, Chemical structures and IP of representative p-type semiconducting polymers, along with the EA of commonly used molecular p-dopants. **b,c**, Absorption spectra of PgBTTT (**b**) and IDTBT (**c**) polymers doped with Na₂S₂O₈ and Magic Blue, showing comparable spectral responses. **d**, Ratio of the neutral peak absorbance before and after doping with

Na₂S₂O₈ and Magic Blue, indicating pronounced bleaching for polymers with IP < 5.2 eV and much less pronounced bleaching for those with IP > 5.2 eV. **e**, Electrical conductivity as a function of IP for the polymers shown in **a**, doped with Na₂S₂O₈ and Magic Blue. Points, mean; error bars, s.d. (not visible); *n* = 10 independent samples.

under those conditions. To confirm the critical role of SO₄^{•-} radicals in the doping process, PBTTT films were immersed in a Na₂S₂O₈ solution containing DMPO, and their electrical conductivity was measured. As shown in Fig. 2d, no change in conductivity was observed, which can be attributed to the scavenging of SO₄^{•-} radicals by DMPO, thereby inhibiting the doping of PBTTT.

Generality of the GAP doping process

Next, we evaluated the generality of the GAP doping process across a range of semiconducting polymers with IPs spanning approximately 1.5 eV, as measured by cyclic voltammetry (Supplementary Fig. 15), and featuring either hydrophilic or hydrophobic side chains. The set included poly(3,3'-bis(tetraethylene glycol methyl)-2,2'-dithiophene-thiophene) (P(g₂T-T)), PgBTTT (a glycolated derivative of PBTTT), poly(3-hexylthiophene) (P3HT), poly(indacenodithiophene-co-benzothiadiazole) (IDTBT), poly[2,3-bis(3-octyloxyphenyl)-5,8-quinoxalinediyl-2,5-thiophenediyl] (PTQ1), poly[4,8-bis(5-(2-ethylhexyl)thiophen-2-yl)benzo[1,2-b:4,5-b']dithiophene-2,6-diyl-alt-(4-(2-ethylhexyl)-3-fluorothieno[3,4-b]thiophene)-2-carboxylate-2,6-diyl] (PTB7-Th), poly[(2,6-(4,8-bis(5-(2-ethylhexyl)-3-fluoro)thiophen-2-yl)-benzo[1,2-b:4,5-b']dithiophene)-alt-(5,5-(1',3'-di-2-thienyl-5',7'-bis(2-ethylhexyl)benzo[1',2'-c:4',5'-c']dithiophene-4,8-dione))] (PBDB-T-2F) and poly(9,9-dioctylfluorene-alt-benzothiadiazole) (F8BT) (Fig. 3a). For comparison, the electron affinities (EAs) of conventional molecular p-dopants such as FeCl₃, F₄TCNQ, Mo(tfd)₃ and tris(4-bromophenyl) ammonium hexachloroantimonate (Magic Blue) are also reported in Fig. 3a. Notably, GAP doping induced optical changes in the absorption spectra that closely resembled those caused by the strong oxidant Magic Blue (EA -5.8 eV)⁵⁰ across all polymers tested (Fig. 3b–d), including the high-IP polymer PBDB-T-2F (IP -5.5 eV) (Supplementary Figs. 16 and 17).

While the spectral changes were less pronounced for higher-IP polymers such as F8BT (IP -5.9 eV; Supplementary Fig. 18), the effect on conductivity was still evident. For example, doping F8BT with

persulfate resulted in a 50–70-fold increase in conductivity, comparable to that achieved with Magic Blue. More broadly, the conductivity of persulfate-doped polymers decreased systematically with increasing IP, from 1,908 ± 114 S cm⁻¹ for P(g₂T-T) (IP -4.4 eV) to 0.29 ± 0.05 S cm⁻¹ for PBDB-T-2F (Fig. 3e). For the latter, this corresponds to a conductivity enhancement of nearly five orders of magnitude compared with its pristine state (Extended Data Fig. 7 and Supplementary Table 2). These findings indicate that the sulfate radical acts as a potent oxidant, at least on par with Magic Blue or Mo(tfd)₃ (EA -5.6 eV)⁵¹, although its standard reduction potential ($E^\circ(\text{SO}_4^{\bullet-}/\text{SO}_4^{2-}) = 2.4 \text{ V}$ versus normal hydrogen electrode)⁵² suggests that its oxidizing power may, in fact, be even greater.

Lateral doping gradient and applicability of the GAP doping process

GAP doping initiates at the gold–OSC interface and propagates laterally, forming a continuous doping gradient across the OSC film. This behaviour is visible macroscopically (Supplementary Video 2) and confirmed by Kelvin probe mapping over millimetre-scale regions under high-concentration (10 mM), long-time doping conditions (up to 10 min; Supplementary Fig. 19). To resolve the gradient at smaller length scales, we performed spatially resolved visible-range absorbance mapping near the gold edge with a 5-μm step (Extended Data Fig. 8 and Supplementary Fig. 20). At high dopant concentrations (10 mM) and short immersion times (4 s), SO₄^{•-} induces rapid bleaching, fully doping the film up to -170 μm from the electrode edge, while regions 4 mm away remain undoped. By contrast, lowering the dopant concentration to 1 mM produces a much more confined lateral diffusion: under these mild conditions, a well-defined -40-μm doping gradient in PBTTT is observed after 4 s. Extending the doping time to 10 s broadens the gradient further, consistent with a laterally advancing doping front. Thicker OSC films exhibit more gradual gradients due to slower persulfate penetration, in agreement with the electrical data showing that lower dopant concentrations or greater film thickness require

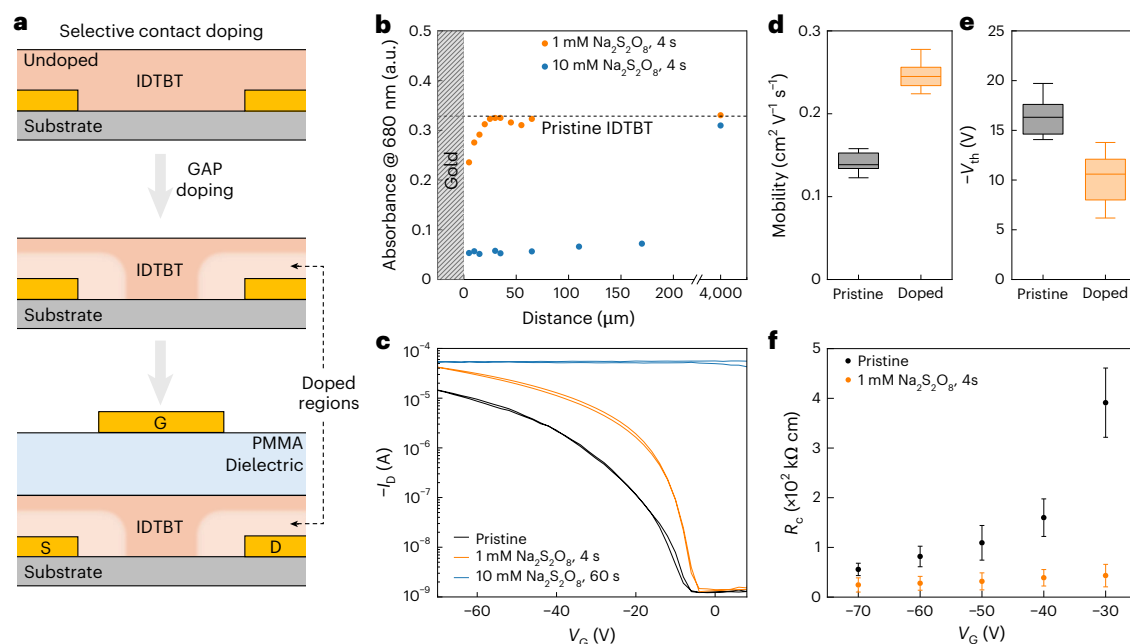


Fig. 4 | Applicability of the GAP doping in OFETs. **a**, Schematic illustration of selective contact doping in OFETs enabled by GAP. **b**, Evolution of the IDTBT absorption peak at 680 nm as a function of distance from the gold electrode edge. **c**, Transfer curves of pristine and contact-doped IDTBT-based OFETs. **d, e**, Mobility (**d**) and threshold voltage (**e**) of pristine and contact-doped IDTBT-based OFETs. The contact-doped devices were treated with 1 mM $\text{Na}_2\text{S}_2\text{O}_8$ for 4 s.

The data were collected from devices with a channel length $L = 50 \mu\text{m}$ and a width $W = 2 \text{ mm}$ at $V_{DS} = -70 \text{ V}$. Boxes, median line and cap indicate 25/75 percentile, mean and minimum/maximum values, respectively; $n = 6$ independent samples. **f**, Contact resistance as a function of gate voltage before and after contact doping. Points represent mean values; error bars show standard deviation; $n = 4$ independent samples.

longer times to reach maximum conductivity (Extended Data Fig. 2 and Supplementary Fig. 8). Raman mapping further corroborates this behaviour (Supplementary Fig. 21). Together, these results demonstrate that GAP doping enables tunable lateral doping fronts ranging from tens of micrometres to several millimetres, depending on dopant concentration, treatment time and film thickness.

Inspired by this distinctive behaviour, we applied GAP doping to OFETs to achieve controlled, contact-proximal doping of the source/drain regions (Fig. 4a). By using a low concentration of $\text{Na}_2\text{S}_2\text{O}_8$ (1 mM) and a short immersion time (4 s), we formed lateral doping gradients in IDTBT, confined to within $\sim 20 \mu\text{m}$ of the electrode edge (Fig. 4b and Supplementary Fig. 22). This selective contact doping resulted in a twofold increase in on-current, while the off-current remained nearly unchanged³³ (Fig. 4c). By contrast, applying a higher concentration of $\text{Na}_2\text{S}_2\text{O}_8$ (10 mM) and longer doping time (60 s) led to complete channel doping and loss of transistor behaviour. This partial doping near the contacts improved overall device performance by mitigating nonideal OFET behaviour, with the field-effect hole mobility increasing from $0.14 \pm 0.02 \text{ cm}^2 \text{V}^{-1} \text{s}^{-1}$ to $0.25 \pm 0.04 \text{ cm}^2 \text{V}^{-1} \text{s}^{-1}$ and the threshold voltage shifting from $-17.36 \pm 2.87 \text{ V}$ to $-9.87 \pm 3.78 \text{ V}$ (Fig. 4d,e, Supplementary Fig. 23 and Supplementary Table 3). The devices remained stable in ambient conditions for at least 10 days without noticeable degradation and retained more than 60% of their initial drain current after 130 days of storage in air (Extended Data Fig. 9). Contact resistance, extracted via the transfer length method (Fig. 4f and Supplementary Fig. 24), revealed that undoped devices exhibit high contact resistance at low gate bias ($391.25 \pm 69.71 \text{ k}\Omega \text{ cm}$ at $V_G = -30 \text{ V}$), which decreased with increasing gate voltage. By contrast, GAP-doped devices showed substantially lower contact resistance even at low gate voltage ($43.29 \pm 22.62 \text{ k}\Omega \text{ cm}$ at $V_G = -30 \text{ V}$). Corresponding output characteristics are shown in Supplementary Fig. 25. Notably, this gradual contact-proximal doping is difficult to achieve with conventional solution-based dopants such as Magic Blue, which tend to uniformly dope the entire channel (Supplementary Fig. 26).

Outlook

In summary, we developed a GAP doping mechanism in which clean gold surfaces promote the homolytic cleavage of persulfate to generate $\text{SO}_4^{\cdot -}$ radicals, as supported by DFT calculations and EPR measurements. These radicals efficiently p-dope a wide range of OSCs with IPs spanning over 1.5 eV, achieving conductivities approaching $1,900 \text{ S cm}^{-1}$. The localized activation of persulfate at the gold–OSC interface induces a lateral doping gradient, confirmed by spectroscopic analysis, enabling selective doping of source and drain regions in OFETs, reducing contact resistance and enhancing mobility. Notably, the spatial resolution of the GAP doping method, on the order of a few tens of micrometres under mild conditions, is comparable to evaporation- or printing-based approaches (Extended Data Table 1), while offering the advantages of simplicity, full solution compatibility and mask-free processing. Importantly, the use of persulfate, an inexpensive and readily available oxidant, makes the GAP doping method scalable, residue-free and cost-effective, providing a practical route for large-area and scalable organic electronics.

Online content

Any methods, additional references, Nature Portfolio reporting summaries, source data, extended data, supplementary information, acknowledgements, peer review information; details of author contributions and competing interests; and statements of data and code availability are available at <https://doi.org/10.1038/s41563-026-02547-0>.

References

- Scaccabarozzi, A. D. et al. Doping approaches for organic semiconductors. *Chem. Rev.* **122**, 4420–4492 (2022).
- Yan, H. & Ma, W. Molecular doping efficiency in organic semiconductors: fundamental principle and promotion strategy. *Adv. Funct. Mater.* **32**, 2111351 (2022).
- Sakai, N. et al. Adduct-based p-doping of organic semiconductors. *Nat. Mater.* **20**, 1248–1254 (2021).

4. Zhang, T. et al. Ion-modulated radical doping of spiro-OMeTAD for more efficient and stable perovskite solar cells. *Science* **377**, 495–501 (2022).
5. Zhu, X. et al. Doping bilayer hole-transport polymer strategy stabilizing solution-processed green quantum-dot light-emitting diodes. *Sci. Adv.* **10**, eado0614 (2024).
6. Tang, C. G. et al. Multivalent anions as universal latent electron donors. *Nature* **573**, 519–525 (2019).
7. Zhao, W., Ding, J., Zou, Y., Di, C. A. & Zhu, D. Chemical doping of organic semiconductors for thermoelectric applications. *Chem. Soc. Rev.* **49**, 7210–7228 (2020).
8. Wang, S. J. et al. Highly efficient modulation doping: a path toward superior organic thermoelectric devices. *Sci. Adv.* **8**, eabl9264 (2022).
9. Lussem, B. et al. Doped organic transistors. *Chem. Rev.* **116**, 13714–13751 (2016).
10. Xu, Y. et al. Doping: a key enabler for organic transistors. *Adv. Mater.* **30**, e1801830 (2018).
11. Paterson, A. F. et al. Water stable molecular n-doping produces organic electrochemical transistors with high transconductance and record stability. *Nat. Commun.* **11**, 3004 (2020).
12. Le, V. N. et al. Improved organic electrochemical transistor stability using solvent degassing and chemical doping. *Nat. Electron.* **8**, 116–126 (2025).
13. Jin, W. et al. Photocatalytic doping of organic semiconductors. *Nature* **630**, 96–101 (2024).
14. Tang, H. et al. A solution-processed n-type conducting polymer with ultrahigh conductivity. *Nature* **611**, 271–277 (2022).
15. Jacobs, I. E. et al. High-efficiency ion-exchange doping of conducting polymers. *Adv. Mater.* **34**, e2102988 (2022).
16. Jacobs, I. E. et al. Structural and dynamic disorder, not ionic trapping, controls charge transport in highly doped conducting polymers. *J. Am. Chem. Soc.* **144**, 3005–3019 (2022).
17. Chen, N. et al. Enhancing electrical conductivity and power factor in poly-glycol-bithienylthienothiophene with oligoethylene glycol side chains through tris (pentafluorophenyl) borane doping. *Adv. Funct. Mater.* **34**, 2400469 (2024).
18. Jacobs, I. E. & Moule, A. J. Controlling molecular doping in organic semiconductors. *Adv. Mater.* **29**, 1703063 (2017).
19. Waldrip, M., Jurchescu, O. D., Gundlach, D. J. & Bittle, E. G. Contact resistance in organic field-effect transistors: conquering the barrier. *Adv. Funct. Mater.* **30**, 1904576 (2019).
20. Cao, L., Ren, C. X. & Wu, T. Recent advances in doped organic field-effect transistors: mechanism, influencing factors, materials, and development directions. *J. Mater. Chem. C* **11**, 3428–3447 (2023).
21. Paterson, A. F. et al. On the role of contact resistance and electrode modification in organic electrochemical transistors. *Adv. Mater.* **31**, e1902291 (2019).
22. Keene, S. T. et al. Hole-limited electrochemical doping in conjugated polymers. *Nat. Mater.* **22**, 1121–1127 (2023).
23. Liu, J. et al. Electrically programmed doping gradients optimize the thermoelectric power factor of a conjugated polymer. *Adv. Funct. Mater.* **34**, 2312549 (2024).
24. Bin, Z. et al. Making silver a stronger n-dopant than cesium via in situ coordination reaction for organic electronics. *Nat. Commun.* **10**, 866 (2019).
25. Tang, C. G. et al. Doped polymer semiconductors with ultrahigh and ultralow work functions for ohmic contacts. *Nature* **539**, 536–540 (2016).
26. Perevedentsev, A. & Campoy-Quiles, M. Rapid and high-resolution patterning of microstructure and composition in organic semiconductors using ‘molecular gates’. *Nat. Commun.* **11**, 3610 (2020).
27. Jacobs, I. E. et al. Direct-write optical patterning of P3HT films beyond the diffraction limit. *Adv. Mater.* **29**, 1603221 (2017).
28. Kim, Y. et al. Enhanced charge injection properties of organic field-effect transistor by molecular implantation doping. *Adv. Mater.* **31**, e1806697 (2019).
29. Darmawan, P. et al. Optimal structure for high-performance and low-contact-resistance organic field-effect transistors using contact-doped coplanar and pseudo-staggered device architectures. *Adv. Funct. Mater.* **22**, 4577–4583 (2012).
30. Khim, D. et al. Control of ambipolar and unipolar transport in organic transistors by selective inkjet-printed chemical doping for high performance complementary circuits. *Adv. Funct. Mater.* **24**, 6252–6261 (2014).
31. Nassyrov, D. et al. Vapour printing: patterning of the optical and electrical properties of organic semiconductors in one simple step. *J. Mater. Chem.* **22**, 4519–4526 (2012).
32. Wang, X. Y. et al. Light-triggered regionally controlled n-doping of organic semiconductors. *Nature* **642**, 599–604 (2025).
33. Ji, Z. et al. Photoexcitation-assisted molecular doping for high-performance polymeric thermoelectric materials. *JACS Au* **4**, 3884–3895 (2024).
34. Xiang, L. et al. Nanoscale doping of polymeric semiconductors with confined electrochemical ion implantation. *Nat. Nanotechnol.* **19**, 1122–1129 (2024).
35. Kolesov, V. A. et al. Solution-based electrical doping of semiconducting polymer films over a limited depth. *Nat. Mater.* **16**, 474–480 (2017).
36. Zhou, Z. et al. Persulfate-based advanced oxidation processes (AOPs) for organic-contaminated soil remediation: a review. *Chem. Eng. J.* **372**, 836–851 (2019).
37. Peng, L. et al. Emulsion polymerization of styrene to polystyrene nanoparticles with self-emulsifying nanodroplets as nucleus. *Langmuir* **41**, 2651–2660 (2025).
38. Guo, X. & Facchetti, A. The journey of conducting polymers from discovery to application. *Nat. Mater.* **19**, 922–928 (2020).
39. Lee, J. H. et al. Radical cation–anion coupling-induced work function tunability in anionic conjugated polyelectrolytes. *Adv. Energy Mater.* **5**, 1501292 (2015).
40. Lee, B. H. et al. Broad work-function tunability of p-type conjugated polyelectrolytes for efficient organic solar cells. *Adv. Energy Mater.* **5**, 1401653 (2015).
41. Stoeckel, M. A. et al. On-demand catalysed n-doping of organic semiconductors. *Angew. Chem. Int. Ed.* **63**, e202407273 (2024).
42. Yamashita, Y. et al. Efficient molecular doping of polymeric semiconductors driven by anion exchange. *Nature* **572**, 634–638 (2019).
43. Liu, T. et al. A polymeric two-in-one electron transport layer and transparent electrode for efficient indoor all-organic solar cells. *Adv. Sci.* **11**, e2405676 (2024).
44. Liu, T. et al. Ground-state electron transfer in all-polymer donor:acceptor blends enables aqueous processing of water-insoluble conjugated polymers. *Nat. Commun.* **14**, 8454 (2023).
45. Herrera-Ordóñez, J. The role of sulfate radicals and pH in the decomposition of persulfate in aqueous medium: a step towards prediction. *Chem. Eng. J. Adv.* **11**, 100331 (2022).
46. Wang, L. L. et al. Undiscovered spin trapping artifacts in persulfate oxidation processes: implications for identification of hydroxyl or sulfate radicals in water. *ACS ES&T Water* **3**, 532–541 (2023).
47. Hu, X. & Zhu, M. Were persulfate-based advanced oxidation processes really understood? Basic concepts, cognitive biases, and experimental details. *Environ. Sci. Technol.* **58**, 10415–10444 (2024).
48. Chen, Y. et al. Selective recovery of precious metals through photocatalysis. *Nat. Sustain.* **4**, 618–626 (2021).
49. Li, R. et al. Radical-involved photosynthesis of AuCN oligomers from Au nanoparticles and acetonitrile. *J. Am. Chem. Soc.* **134**, 18286–18294 (2012).

50. Hofmann, A. I. et al. Chemical doping of conjugated polymers with the strong oxidant Magic Blue. *Adv. Electron. Mater.* **6**, 2000249 (2020).
51. Qi, Y. et al. Use of a high electron-affinity molybdenum dithiolene complex to p-dope hole-transport layers. *J. Am. Chem. Soc.* **131**, 12530–12531 (2009).
52. Das, T. N., Huie, R. E. & Neta, P. Reduction potentials of $\text{SO}_3^{\cdot-}$, $\text{SO}_5^{\cdot-}$, and $\text{S}_4\text{O}_6^{\cdot 3-}$ radicals in aqueous solution. *J. Phys. Chem. A* **103**, 3581–3588 (1999).
53. Shi, Y. J., Liu, J., Hu, Y. Y., Hu, W. P. & Jiang, L. Effect of contact resistance in organic field-effect transistors. *Nano Select* **2**, 1661–1681 (2021).

Publisher's note Springer Nature remains neutral with regard to jurisdictional claims in published maps and institutional affiliations.

Open Access This article is licensed under a Creative Commons Attribution 4.0 International License, which permits use, sharing, adaptation, distribution and reproduction in any medium or format, as long as you give appropriate credit to the original author(s) and the source, provide a link to the Creative Commons licence, and indicate if changes were made. The images or other third party material in this article are included in the article's Creative Commons licence, unless indicated otherwise in a credit line to the material. If material is not included in the article's Creative Commons licence and your intended use is not permitted by statutory regulation or exceeds the permitted use, you will need to obtain permission directly from the copyright holder. To view a copy of this licence, visit <http://creativecommons.org/licenses/by/4.0/>.

© The Author(s) 2026

Methods

Materials

PBTTT⁵⁴ and its glycolated derivative PgBTTT⁵⁵ were synthesized according to previous reports. P3HT, LiTFSI, persulfate salts, DDT, DMPO, Magic Blue, F₄TCNQ, poly(methyl methacrylate) (PMMA) and organic solvents such as acetonitrile, 1,2-dichlorobenzene, chloroform and ethanol were purchased from Sigma-Aldrich. P(g₄T-T), IDTBT, PTB7-Th and PBDB-T-2F were purchased from I-Material. PTQ1 was purchased from Solarmer Energy, while F8BT was purchased from Ossila.

Sample preparation

PBTTT was dissolved in 1,2-dichlorobenzene (10 mg ml⁻¹) and spin-coated onto the substrates at 2,000 rpm. The films were annealed at 180 °C for 20 min in a N₂-filled glovebox and then slowly cooled to room temperature. Under these conditions, PBTTT films had a typical thickness of ~30 nm. Thicker films were obtained from a more concentrated solution (20 mg ml⁻¹), with spin-coating at 1,000 rpm yielding ~100 nm and at 2,000 rpm yielding ~70 nm. All other p-type polymers were dissolved in either 1,2-dichlorobenzene or chloroform (10 mg ml⁻¹) and spin-coated following the same procedure used for PBTTT.

Doping process

Na₂S₂O₈ was mixed with LiTFSI in acetonitrile at a molar ratio of 1:10. Typically, a 10-mM dopant solution was prepared by dissolving Na₂S₂O₈ (4.76 mg, 0.02 mmol) and LiTFSI (57.4 mg, 0.2 mmol) in 2 ml of acetonitrile. The resulting dopant solution was sonicated at room temperature for 20 min. A freshly prepared dopant solution was used for each doping experiment. The polymer films were immersed in the dopant solution, rinsed with deionized water, and subsequently dried under N₂. Doping with Magic Blue and F₄TCNQ was performed following previously reported procedures^{42,50}.

Electrical characterization

Electrical conductivity measurements were performed using a four-probe set-up with a channel width/length of 5 mm/0.5 mm. The results were validated using devices with longer channels (5 mm/1 mm and 5 mm/2 mm; Supplementary Fig. 27). Seebeck coefficient measurements were performed in a glovebox using a pair of Peltier elements to generate the temperature difference. All measurements were conducted using a Keithley 4200-SCS semiconductor characterization system.

For the gold electrode, 5-nm Cr and 50-nm Au were thermally evaporated onto a cleaned glass substrate and patterned using photolithography. The DDT-modified gold was prepared by immersing bare gold electrodes in a DDT solution (0.25 vol% in ethanol) for 3 days, followed by ethanol washing. DDT modification was confirmed by contact angle measurements (Supplementary Fig. 28). Aluminium, silver, chromium and copper electrodes (50 nm) were thermally evaporated onto glass substrates, using a 5-nm Cr adhesion layer, and subsequently patterned by photolithography. The ITO electrode, approximately 150 nm thick, was purchased from Zhuhai Kaivo Optoelectronic Technology and patterned by laser etching. The sheet resistance of Au and ITO electrodes was about 1 and 7 Ω sq⁻¹, respectively.

Optical characterization

PBTTT films were prepared by spin-coating the polymer solution on glass substrates with or without gold strips. Gold was thermally evaporated onto cleaned glass and patterned by photolithography, with a 500-μm spacing between adjacent lines. The absorbance spectra were recorded using a ultraviolet–visible–near-infrared spectrophotometer (PerkinElmer Lambda 950) with a 2-nm step. Spatially resolved absorbance mapping was performed in transmission mode using a Nikon Eclipse L200N (10× objective) coupled to a fibre-optic spectrophotometer (50-μm fibre, QE PRO-ABS, Ocean Optics). The microscope's built-in halogen lamp served as the light source. The recorded spectra

were referenced against an uncoated glass substrate. All other p-type polymer films were deposited and characterized following the same procedure used for PBTTT.

XPS and UPS spectroscopy

XPS and UPS measurements were performed on PBTTT films spin-coated onto ITO- or gold-coated glass substrates using a Scienta ESCA 200 system equipped with a SES 200 electron analyser under ultrahigh vacuum conditions (1 × 10⁻¹⁰ mbar). A monochromatic Al Kα X-ray source (1,486.6 eV) and a helium discharge lamp (21.22 eV) were used for XPS and UPS measurements, respectively. All spectra were collected at normal emission and calibrated by a sputter-cleaned Au film, with the Fermi level set to 0 eV and the Au 4f peak at 84.0 eV.

EPR measurements

The EPR spectra were acquired using a SPINSCAN X spectrometer by Linev Systems in the dark at room temperature. The modulation frequency, microwave power and microwave frequency were set to 100 kHz, 1 mW and 9.46 GHz, respectively. For polaron measurements in doped PBTTT films, the PBTTT solution was spin-coated onto poly(ethylene terephthalate) (PET) or gold-coated PET substrates. Then, the PBTTT films were cut into pieces measuring 2 × 20 mm and placed into an N₂-filled quartz tube. The spectra were recorded with a modulation width of 0.7 mT and a sweep time of 60 s. To test for SO₄^{•-} radicals in solution, 100 μl of DMPO was added to the persulfate solution. After 5 min, the mixtures were transferred into capillaries, which were sealed at the bottom and inserted into an N₂-filled quartz tube. EPR spectra were recorded with a modulation width of 0.1 mT and a sweep time of 300 s. The EPR signals of the DMPO adducts were simulated using the open-source software package EasySpin (version 6.0.10).

GIWAXS measurements

GIWAXS measurements were performed on PBTTT films spin-coated onto silicon or gold-coated silicon substrates. The diffraction patterns were collected at an X-ray energy of 11.06 eV with an incidence angle of 0.12° at Beamline 9A in the Pohang Accelerator Laboratory. All samples were measured under vacuum with an exposure time of 10 s.

Kelvin probe

Work function mapping was performed using a scanning Kelvin Probe (SKP5050) under ambient conditions. The measurement was calibrated using highly ordered pyrolytic graphite (work function 4.6 eV), with a scanning step of 0.4 mm.

QCM-D measurements

Quartz crystals coated with gold (QSX301, Biolin Scientific) or SiO₂ (QSX303, Biolin Scientific) were used as substrates for PBTTT deposition. The frequency and dissipation of the QCM crystals were recorded using a QSense Analyzer (Biolin Scientific). The pristine crystal served as a reference to the reported frequency and dissipation shifts, which were recorded following PBTTT coating and subsequent contact with the dopant solution (10 mM Na₂S₂O₈ in acetonitrile).

Cyclic voltammetry

Cyclic voltammetry was performed using a BioLogic SP-200 potentiostat. A 0.1-M solution of Bu₄NPF₆ in acetonitrile was used as electrolyte. Polymer films were spin-coated onto clean gold substrates, which served as the working electrode. A platinum mesh and an Ag/AgCl (saturated) electrode were used as the counter and reference electrodes. The potential was calibrated using a standard ferrocene sample. All scans were recorded at a scan rate of 50 mV s⁻¹.

Raman spectroscopy

Raman spectra were collected at room temperature using a Renishaw InVia Reflex confocal Raman spectrometer equipped with a Leica

50× objective (numerical aperture 0.50), a 2,400 grooves mm⁻¹ grating and an Ar-ion 532-nm laser (100 mW at the source). A Renishaw charge-coupled device camera was used as the detector. Spectra were acquired in static mode, covering the spectral range 583–1,760 cm⁻¹. The exposure time was 1 s, with one accumulation for pristine samples and four accumulations for doped samples. This configuration provides a spectral resolution better than 1 cm⁻¹ and a spatial resolution of ~1.3 μm. The spectrometer was calibrated to the first-order Si vibrational mode at 520.6 cm⁻¹. For Raman mapping, a step size of 2 μm was used, with mapped regions including both on- and off-electrode areas. For each point, the intensity ratio P_1/P_2 (Supplementary Fig. 21) is reported after applying a constant subtraction to set the signal to zero at 1,228 cm⁻¹.

Computational details

DFT-based simulations were performed with the CP2K/Quickstep package, using a hybrid Gaussian and plane wave method⁵⁶. A triple quality TZVP Gaussian basis set was used for the Au and Na atoms, and a triple quality aug-TZVP Gaussian basis set augmented with a diffuse function was used for all other atoms⁵⁷. The Goedecker–Teter–Hutter pseudopotentials⁵⁸, together with a 400-Ry plane wave cut-off, were used to expand the densities obtained with the Perdew–Burke–Ernzerhof⁵⁹ exchange–correlation density functional, and van der Waals forces are taken into account with the Grimme D3 Method⁶⁰. Only the gamma point was considered in a supercell approach. Periodic boundary conditions are applied in all directions of space.

Surface model. The gold (111) surface was constructed using a slab model with three Au layers, yielding a 17.31 Å × 14.99 Å surface unit cell (108 Au atoms). A 35-Å vacuum region between the slabs was used to minimize unrealistic interactions between the slabs. Only the gamma point was considered in a supercell approach. Periodic boundary conditions were applied in all directions of space. The slab charge was neutralized, including two Na cations to balance the S₂O₈²⁻ negative charge. The transition state of the homolytic cleavage of S₂O₈²⁻ was identified by tracking the energy as a function of the O–O peroxo bond distance, while the transition state of the electron transfer was calculated by considering the optimized geometries of the reactants with the electronic configuration of the products. Molecular graphics were produced by the CHEMCRAFT graphical package⁶¹.

Gibbs free energy profile. Potential energy as obtained by the self-consistent field (SCF) procedure at zero Kelvin is adopted as energy reference. Entropic and enthalpic contributions were evaluated on the analysed reactions without the gold surface by performing the frequency calculation of the molecular species at 298.15 K and 1 atm as implemented in the G16 code⁶². G16 calculations were performed at the M06 hybrid functional level⁶³, using the standard all-electron 6–311+G** basis set for all atoms. The enthalpic and entropic contributions were then ‘appended’ to the SCF energy profile of the analogue reactions that occurred on the gold surface to obtain the Gibbs free energy profile. Solvation contribution to the energy profile was evaluated within the PCM approach⁶⁴ for molecular species using acetonitrile ($\epsilon = 38.8$ D) as a prototypical solvent. For the reaction on the gold surface, the solvent effect was taken into account by considering the solvation energy values associated with half-cavity formation.

OFET fabrication and characterization. Top-gate, bottom-contact OFETs were fabricated on glass substrates with photolithographically defined Cr/Au electrode (5/50 nm thickness), as schematically illustrated in Supplementary Fig. 29. IDTBT was then deposited by spin-coating from 7 mg ml⁻¹ chlorobenzene solution at 1,500 rpm for 40 s, followed by thermal annealing at 100 °C for 30 min to remove residual solvent. The contact doping was performed using

the above-described method. Subsequently, a PMMA dielectric layer ($M_w = 120$ kDa, 80 mg ml⁻¹ in butylacetate) was spin-coated onto the IDTBT layer at 3,000 rpm for 40 s, followed by drying on a hotplate at 80 °C for 2 h. A 40-nm-thick aluminium top gate was then thermally evaporated through a shadow mask to complete the device. All transistor characteristics were measured in air using a Keithley 4200-SCS semiconductor characterization system. A summary of methods used to spatially control doping of OSCs is provided in Extended Data Table 1 (refs. 26,28–35,65–68).

Data availability

The data supporting the findings of this study are available within the Article and its Supplementary Information. Source data are provided with this paper.

References

- Kline, R. J. et al. Critical role of side-chain attachment density on the order and device performance of polythiophenes. *Macromolecules* **40**, 7960–7965 (2007).
- Hallani, R. K. et al. Regiochemistry-driven organic electrochemical transistor performance enhancement in ethylene glycol-functionalized polythiophenes. *J. Am. Chem. Soc.* **143**, 11007–11018 (2021).
- Kuhne, T. D. et al. CP2K: an electronic structure and molecular dynamics software package—Quickstep: efficient and accurate electronic structure calculations. *J. Chem. Phys.* **152**, 194103 (2020).
- VandeVondele, J. & Hutter, J. Gaussian basis sets for accurate calculations on molecular systems in gas and condensed phases. *J. Chem. Phys.* **127**, 114105 (2007).
- Goedecker, S., Teter, M. & Hutter, J. Separable dual-space Gaussian pseudopotentials. *Phys. Rev. B* **54**, 1703–1710 (1996).
- Perdew, J. P., Burke, K. & Ernzerhof, M. Generalized gradient approximation made simple. *Phys. Rev. Lett.* **77**, 3865–3868 (1996).
- Grimme, S., Antony, J., Ehrlich, S. & Krieg, H. A consistent and accurate ab initio parametrization of density functional dispersion correction (DFT-D) for the 94 elements H–Pu. *J. Chem. Phys.* **132**, 154104 (2010).
- ChemCraft—Graphical Software for Visualization of Quantum Chemistry Computations version 1.8, build 682 (ChemCraft); <https://www.chemcraftprog.com>
- Gaussian 16 Rev. B.01 (Gaussian, 2016).
- Zhao, Y. & Truhlar, D. G. The M06 suite of density functionals for main group thermochemistry, thermochemical kinetics, noncovalent interactions, excited states, and transition elements: two new functionals and systematic testing of four M06-class functionals and 12 other functionals. *Theor. Chem. Acc.* **120**, 215–241 (2008).
- Tomasi, J., Mennucci, B. & Cammi, R. Quantum mechanical continuum solvation models. *Chem. Rev.* **105**, 2999–3093 (2005).
- Singh, S. et al. Reduction of contact resistance by selective contact doping in fullerene n-channel organic field-effect transistors. *Appl. Phys. Lett.* **102**, 153303 (2013).
- Lu, G. et al. Moderate doping leads to high performance of semiconductor/insulator polymer blend transistors. *Nat. Commun.* **4**, 1588 (2013).
- Tiwari, S. P. et al. Pentacene organic field-effect transistors with doped electrode–semiconductor contacts. *Org. Electron.* **11**, 860–863 (2010).
- Baeg, K.-J. et al. Charge injection engineering of ambipolar field-effect transistors for high-performance organic complementary circuits. *ACS Appl. Mater. Interfaces* **3**, 3205–3214 (2011).

Acknowledgements

We thank M. Cambiaggio and M. Caironi (Italian Institute of Technology) for helpful discussions on OFET measurements. This work was financially supported by the Knut and Alice Wallenberg Foundation (grant nos. 2021.0058 and 2022.0034), including support from the Wallenberg Wood Science Center (WWSC) and the Wallenberg Initiative Materials Science for Sustainability (WISE); the Swedish Research Council (grant nos. 2020-03243, 2022-04053 and 2022-04553); the European Commission through the MSCA-ITN project HORATES (grant no. GA-955837) and the MSCA-IF project IONIC (grant no. 101148701); the European Research Council through the ERC Consolidator grant project INFER (grant no. 101125879); and the Swedish government's Strategic Research Area in Materials Science on Functional Materials at Linköping University (faculty grant no. SFO-Mat-LIU 2009-00971). H.Y.W. acknowledges financial support from the National Research Foundation of Korea (grant no. RS-2025-24683763). A. Motta acknowledges the CINECA award no. HP10CL5217 2024 under the ISCRA initiative for computational resources.

Author contributions

T.L. and S.F. conceived and designed the project. T.L. and M.S. tested the electric, optical and EPR measurements. Z.L., F.Z. and M.F. recorded and analysed the UPS and XPS spectra. S.Y.J., C.-Y.Y. and H.Y.W. measured and analysed the GIWAXS data. Q.H. and M.H. synthesized PBTTT. C.K. and I.M. synthesized P_gBTTT. T.P.A.v.d.P. and T.L. performed the QCM-D and absorbance-mapping measurements. G.G.G. and A.M. acquired and analysed the Raman data. T.L. and W.J.

fabricated and tested the OFETs. A. Motta performed the DFT calculations. T.L. and S.F. wrote the manuscript. All authors contributed to the discussion and manuscript preparation.

Funding

Open access funding provided by Linköping University.

Competing interests

The authors declare no competing interests.

Additional information

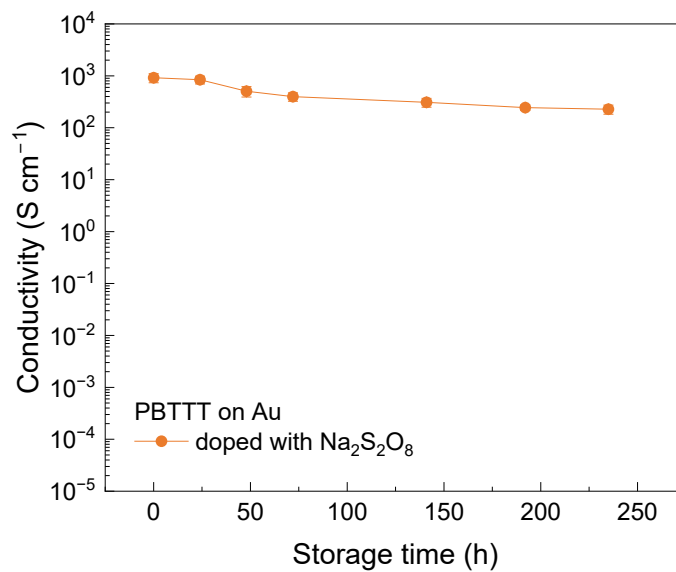
Extended data is available for this paper at <https://doi.org/10.1038/s41563-026-02547-0>.

Supplementary information The online version contains supplementary material available at <https://doi.org/10.1038/s41563-026-02547-0>.

Correspondence and requests for materials should be addressed to Simone Fabiano.

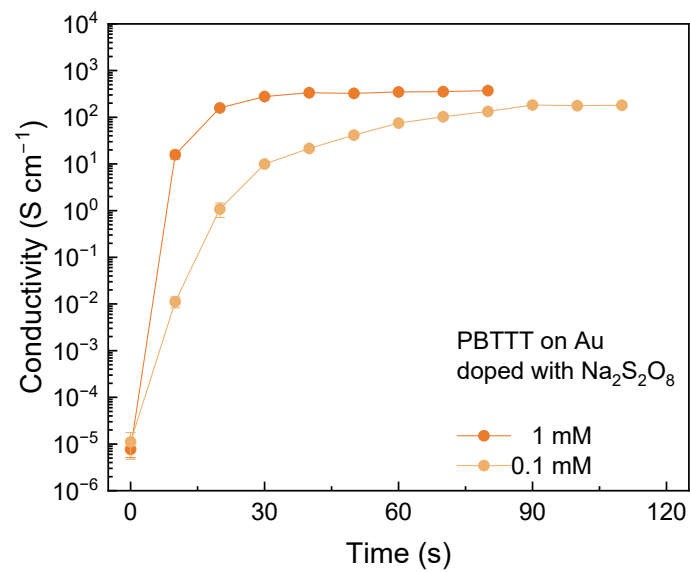
Peer review information *Nature Materials* thanks Sasikumar Mayarambakam and Jian Pei and the other, anonymous, reviewer(s) for their contribution to the peer review of this work.

Reprints and permissions information is available at www.nature.com/reprints.

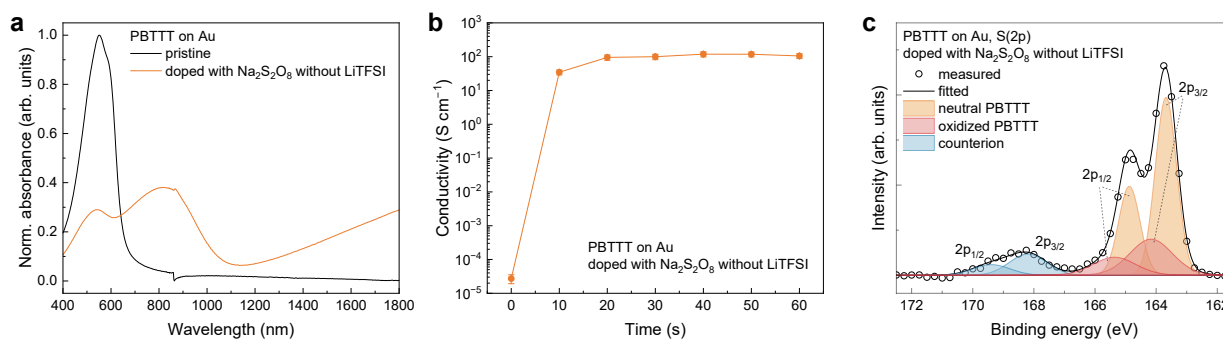


Extended Data Fig. 1 | Ambient stability of GAP doped PBTTT. Electrical conductivity of PBTTT films doped with $\text{Na}_2\text{S}_2\text{O}_8$ in the presence of LiTFSI, measured over extended storage under ambient laboratory conditions

($\approx 22^\circ\text{C}$, $\sim 40\%$ RH). The conductivity remained well above 200 S cm^{-1} after 235 h in air. Points represent mean values; error bars show standard deviation (s.d., not visible at this scale); $n = 10$ independent samples.

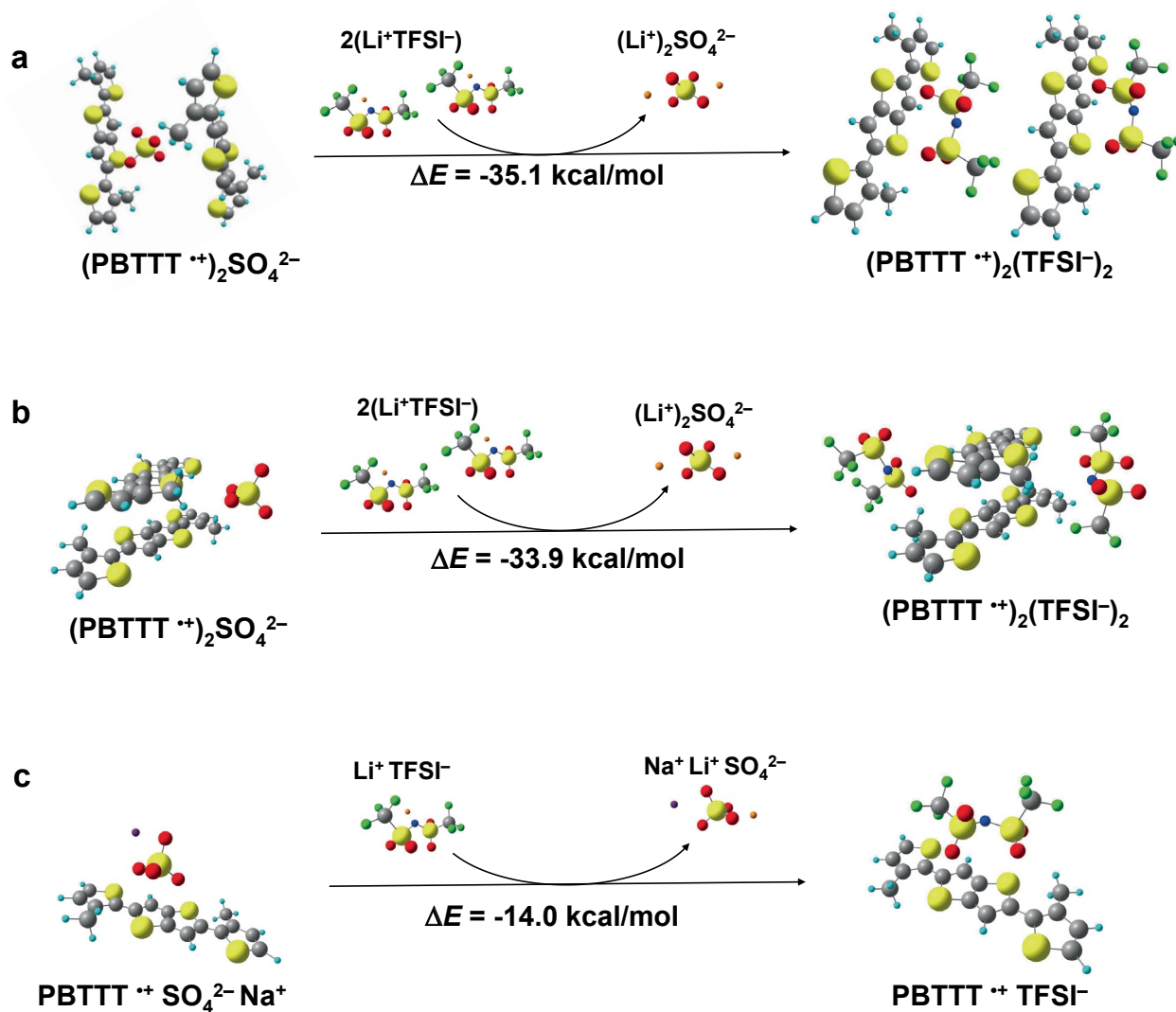


Extended Data Fig. 2 | Effect of persulfate concentration. Electrical conductivity of PBTTT films measured on bare gold electrodes after doping with Na₂S₂O₈ in the presence of LiTFSI as the counterion. Points represent mean values; error bars show standard deviation (s.d., not visible at this scale); n = 10 independent samples.



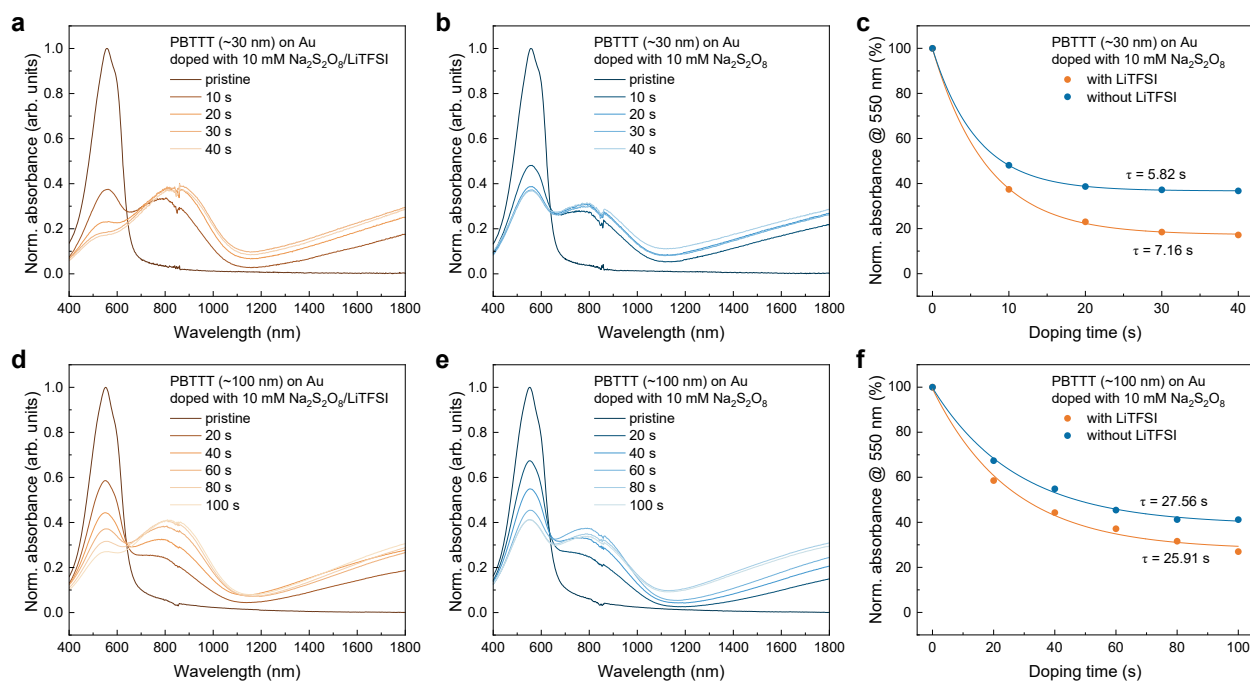
Extended Data Fig. 3 | GAP doping in the absence of counterions. **a**, Absorption spectra and **b**, electrical conductivity of PBTTT films on gold doped with Na₂S₂O₈ in the absence of LiTFSI. Points represent mean values; error bars show standard deviation (s.d., not visible at this scale); n = 10 independent samples. **c**, XPS S(2p)

spectrum of PBTTT on gold doped with Na₂S₂O₈ without LiTFSI. The doping level is estimated to be ≈29% from the ratio of the oxidized PBTTT signal to the total PBTTT S(2p) area.

**Extended Data Fig. 4 | Energetics of counterion exchange in doped PBTTT.**

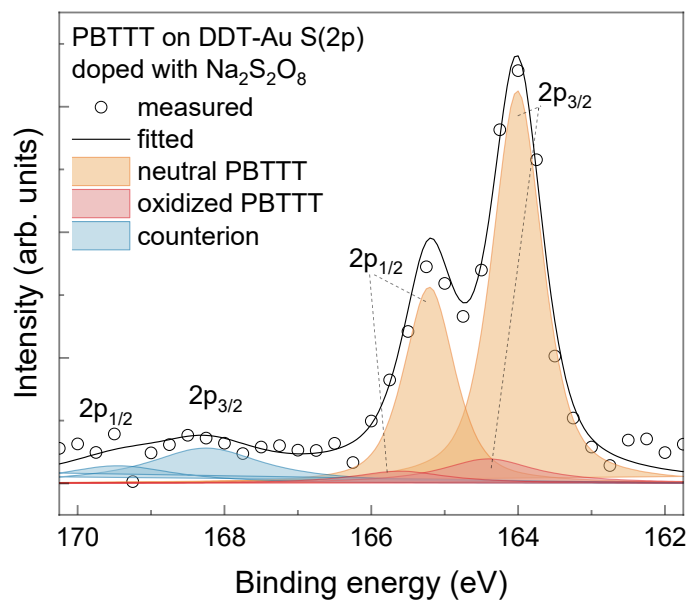
Ion exchange process between $(\text{PBTTT}^{++})_2\text{SO}_4^{2-}$ species and Li^+TFSI^- . The ion-exchange energetics were calculated using DFT (M06 hybrid functional with the 6-311 + G** basis set) as implemented in Gaussian 16. Geometry optimizations were performed without constraints, and solvent effects (acetonitrile) were included using the PCM model. Conformations of $(\text{PBTTT}^{++})_2\text{SO}_4^{2-}$ and

$\text{PBTTT}^{++}\text{TFSI}^-$ were taken from literature (see Ref. 42). Three conformations were considered: (a) counterion intercalated between two PBTTT^{++} molecules, (b) counterion located on the lateral side of two stacked PBTTT^{++} molecules, and (c) ion exchange involving only a single PBTTT^{++} molecule. In all cases, replacement of SO_4^{2-} by TFSI^- was found to be exothermic, in agreement with the experimental results.

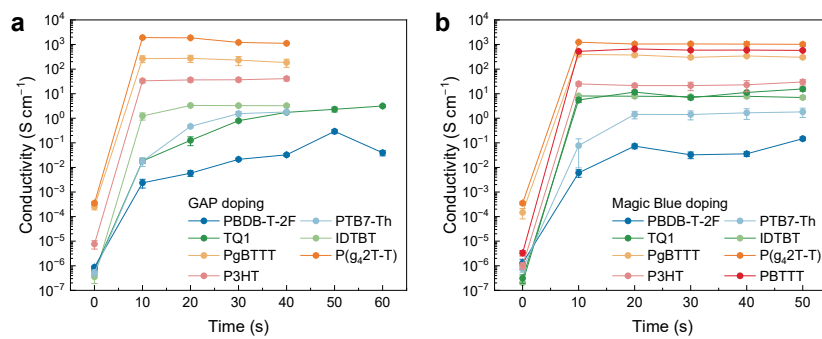
**Extended Data Fig. 5 | Kinetics of GAP doping with and without LiTFSI.**

a, Absorbance evolution of thin PBTTT films (~30 nm) doped with $\text{Na}_2\text{S}_2\text{O}_8$ in the presence of LiTFSI, and **(b)** corresponding evolution without LiTFSI. **c**, Decay fitting of the neutral peak absorbance for the thin films. **d**, Absorbance evolution of thick PBTTT films (~100 nm) doped with $\text{Na}_2\text{S}_2\text{O}_8$ in the presence of LiTFSI,

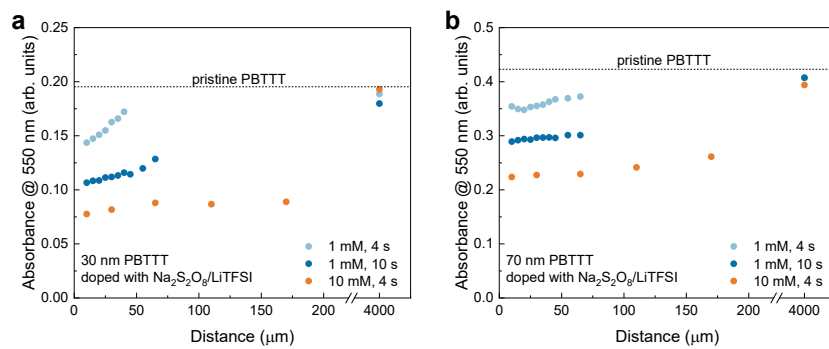
and **(e)** corresponding evolution without LiTFSI. **f**, Decay fitting of the neutral peak absorbance for the thick films. In both thin and thick films, the neutral peak exhibits similar decay times under $\text{Na}_2\text{S}_2\text{O}_8$ doping with or without LiTFSI, indicating that LiTFSI does not affect the doping kinetics.



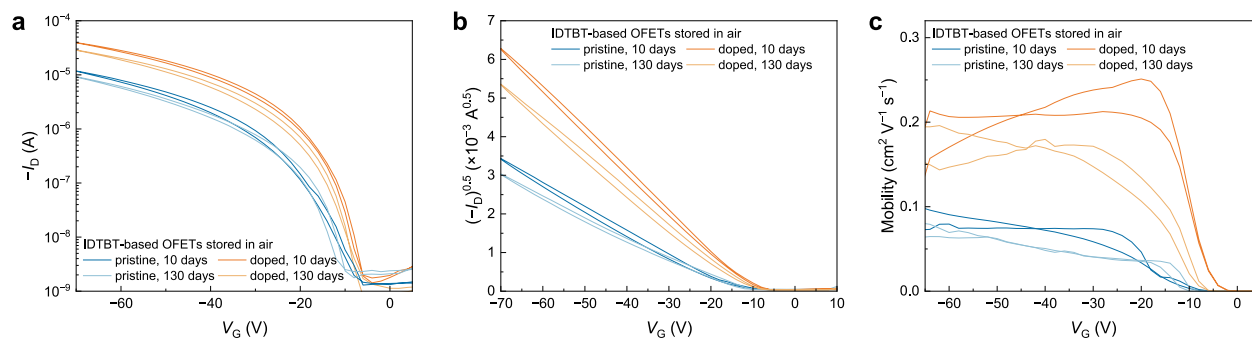
Extended Data Fig. 6 | Doping level of PBTTT on DDT-modified gold. XPS S(2p) spectrum of PBTTT deposited on DDT-treated gold and doped with $\text{Na}_2\text{S}_2\text{O}_8/\text{LiTFSI}$. The doping level is estimated to be 12% based on the ratio of the oxidized PBTTT peak area to the total PBTTT S(2p) signal.



Extended Data Fig. 7 | Electrical conductivity of GAP-doped polymers and comparison with Magic Blue. Electrical conductivity of representative p-type polymers doped with (a) GAP and (b) Magic Blue. Points represent mean values; error bars show standard deviation (s.d., not visible at this scale); n = 10 independent samples.



Extended Data Fig. 8 | Spatial doping gradient in PBTTT films. Evolution of the neutral PBTTT absorption peak at 550 nm as a function of distance from the gold edge for (a) thin (~30 nm) and (b) thick (~70 nm) films. The data were extracted from Supplementary Fig. 20.



Extended Data Fig. 9 | Stability of GAP-doped IDTBT-based OFETs. (a) Transfer, (b) $I_D^{0.5}$, and (c) saturation mobility curves of pristine and doped IDTBT OFETs ($L = 50 \mu\text{m}$, $W = 2 \text{ mm}$, $V_{DS} = -70 \text{ V}$) monitored for up to 130 days of storage under ambient laboratory conditions ($\approx 22^\circ\text{C}$, $\sim 40\% \text{ RH}$). Doping conditions: 1 mM $\text{Na}_2\text{S}_2\text{O}_8$ for 4 s.

Extended Data Table 1 | Summary of methods for spatially controlled doping of OSCs

Method	Doping condition	Direction	Resolution	Ref.
Thermal evaporation	vacuum	Lateral	25 μm	65
Thermal evaporation	vacuum	Lateral	50 μm	28
Thermal evaporation	vacuum	Lateral	300 μm	66
Thermal evaporation	vacuum	Lateral	50 μm	29
Thermal evaporation	vacuum	Lateral	N.A.	67
Printing	inkjet printer	Lateral	20 μm	30
Printing	spray printer	Lateral	1 mm	68
Printing	vapor printer	Lateral	1 mm	31
Molecular gates	heat, solvent vapor or laser	Lateral	18 μm	26
Electrochemical ion implantation	electric field	Lateral	53 nm	34
Light-triggered	light illumination	Lateral	1 μm	32
Photoexcitation-assisted	light illumination	Lateral	1 μm	33
Solution-processed	room temperature in ambient	Vertical	N.A.	35
Solution-processed	room temperature in ambient	Lateral	$\sim 20\mu\text{m}$	This work